

Ballistic resistance of double-layered armor plates

X. Teng^{*,1}, T. Wierzbicki, M. Huang

Impact and Crashworthiness Lab, Room 5-218, Massachusetts Institute of Technology, Cambridge, MA 02139, USA

Received 20 July 2007; received in revised form 3 January 2008; accepted 7 January 2008

Available online 12 February 2008

Abstract

In this paper, the ballistic resistance of double-layered steel shields against projectile impact at the sub-ordnance velocity is evaluated using finite element simulations. Four types of projectiles of different weight and nose shapes are considered, while armor shields consist of two layers of different materials. In a previous study of the same authors, it was shown that a double-layered shield of the same metal was able to improve the ballistic limit by 7.0–25.0% under impact by a flat-nose projectile, compared to a monolithic plate of the same weight. Under impact by a conical-nose projectile, a double-layered shield is almost as capable as a monolithic plate. The present paper extends the analysis to double-layered shields with various metallic material combinations. The study reveals that the best configuration is the upper layer of high ductility and low strength material and the lower layer of low ductility and high strength material. This configuration results in some 25% gain in the ballistic limit under moderate detrimental impact. This research helps clarify the long standing issue of the ballistic resistance of the multi-layered armor configuration.

© 2008 Elsevier Ltd. All rights reserved.

Keywords: Projectile; Perforation; Ductility; Impact failure; Fracture criterion

1. Introduction

An optimization of metal shields against projectile impact has long been of practical interest in military and civilian applications. This paper proposes a double-layered configuration that consists of two parallel layers as a potential improvement over a monolithic plate. Although a lot of investigations have been done on the perforation resistance of monolithic plates experimentally, numerically, and theoretically. Limited studies on multi-layered metal shields were reported in the open literature.

On the basis of a series of tests, Marom and Bodner [1] found that multi-layered beams were more effective in resisting perforation than monolithic beams of the same weight under projectile impact. Corran et al. [2] showed experimentally that a double/triple-layered shield was superior in ballistic resistance to a monolithic plate if the total

thickness exceeded a critical value. An opposite conclusion was obtained by Radin and Goldsmith [3]. They performed normal impact tests on multi-layered shields of a wide range of thickness. The ballistic limit of a monolithic plate was always higher than that of a multiple-layered shield of the same total thickness. This finding was confirmed by Almohandes et al. [4] through an extensive experimental program on steel plates of various configurations impacted by standard 7.62mm bullet projectiles. Dey et al. [5,6] recently reported a comprehensive experimental and numerical study on the perforation resistance of double-layered steel armor plates. They found that in the case with a blunt-nose projectile, the ballistic limit of a double-layered shield was 30% higher than that of the monolithic case.

The above literature review indicates that the protection effectiveness of multi-layered shields remains a subject of debate. Note that in those studies various projectiles and target materials were considered. In this connection, two questions can be posed: Under what type of projectile impact would a multi-layered shield be superior in the perforation resistance to a monolithic plate of the same

*Corresponding author. Tel.: +1 617 253 2104; fax: +1 617 253 1962.

E-mail address: xteng@alum.mit.edu (X. Teng).

¹Currently with Hess Corporation.

weight? Between ductility and strength, which property is more important for the perforation resistance against projectile impact?

Previous research has revealed that different failure modes may be developed in a target by changing impact conditions, e.g. see Teng and Wierzbicki [7], and Børvik et al. [8,9]. A failure mode with higher energy absorption can significantly improve the ballistic resistance of a shield. By replacing a monolithic plate with a double-layered plate, the bending action can be enhanced and thus the double-layered plate may undergo considerable deformation before fracture. By defining two different grades of metals of various strength and ductility for two layers, the performance of a double-layered shield can be further improved.

The objective of the present paper is to evaluate the effectiveness of the double-layered configuration against projectile impact. In practical applications, a variety of projectiles including heavy fragments generated from improvised explosive devices (IEDs) and light bullet projectiles typical for small arms may be encountered. Since a shield would behave differently under the impact of various projectiles, four types of projectiles of different weight and nose shapes are considered in this paper.

For each projectile–target system, a thorough parametric study should be conducted to determine the ballistic resistance of the shields. A corresponding experimental study could be overly expensive. As an alternative, commercial finite element codes are able to fulfill this task equipped with a suitable fracture model. In this paper, all of perforation cases are simulated using ABAQUS/explicit. Numerical modeling provides an insight into failure mechanisms and the number of necessary tests is reduced. The paper concludes by pointing out the advantage of the double-layered configuration over the monolithic plate.

2. Problem formulation

The objective of the present paper is to assess the ballistic resistance of an armor plate consisting of two layers of

metallic materials with different mechanical characteristics. The performance of such a system will be compared to that of a monolithic plate. For that purpose several impact scenarios are considered by varying the nose shape and mass of the projectile, the impact velocity and the relative strength and ductility of the constituent layers. Fig. 1 shows a double-layered target shield of the total thickness of 12 mm studied in this paper.

To design light armor shields against fragment impact, U.S. military standard MIL-P-46593A specifies three types of fragment simulating projectiles (FSPs) of the weight 44, 207, and 830 g [10]. All these FSPs are of cylindrical shape and chisel nose. In this paper, four types of cylindrical projectiles are under consideration, see Fig. 2. There are two weights of different orders of magnitude: 200 and 30 g. Two types of projectile noses are defined: flat-nose and conical-nose, which represent two limiting cases.

There are totally 16 impact scenarios with different combinations of the four metal shields and the four projectiles. Also, the impact velocity of the projectiles varies from $V_0 = 400$ to 800 m/s. The perforation resistance of the four shields is evaluated by comparing their residual velocities.

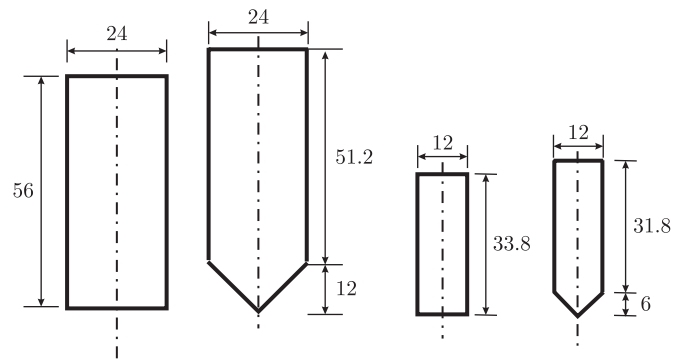


Fig. 2. Four cylindrical projectiles considered in this study (units: mm).

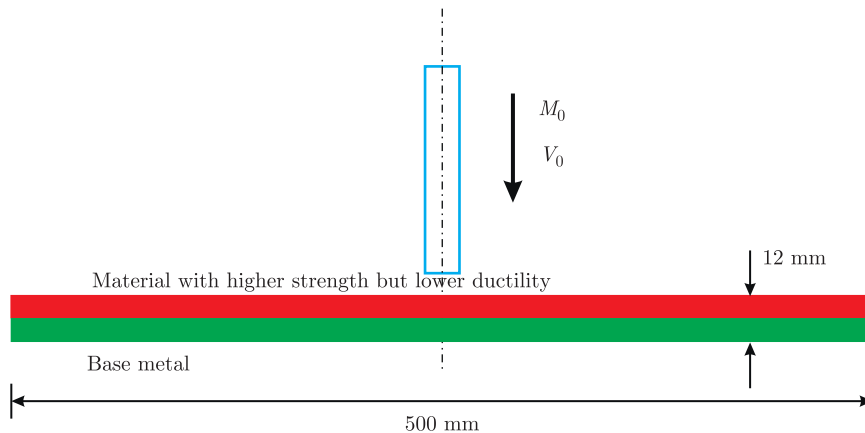


Fig. 1. A double-layered shield with two different materials.

Table 1
Material constants for Wieldox 460 E steel

E (GPa)	ν	ρ (kg/m ³)	$\dot{\epsilon}_0$ (s ⁻¹)	C
200	0.33	7850	5.00×10^{-4}	0.0123
c_v (J/kg K)	T_m (K)	T_0 (K)	m	A (MPa)
452	1800	293	0.94	490
B (MPa)	n	D_1	D_2	D_3
383	0.45	0.0705	1.732	-0.54

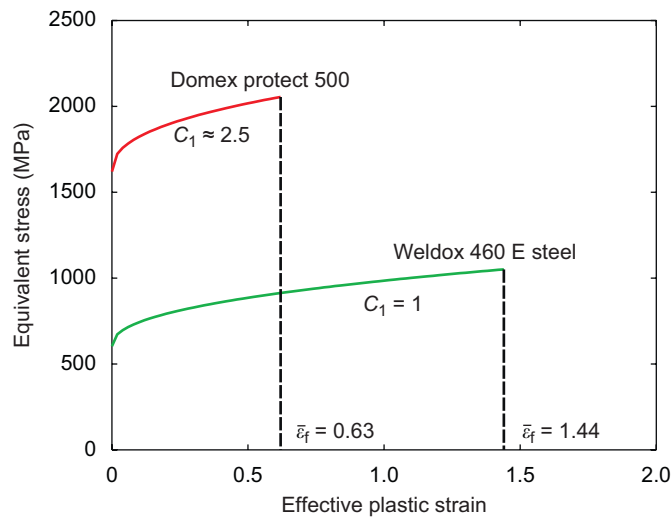


Fig. 3. True stress–strain curves of two types of armor steels studied in this paper. $\bar{\epsilon}_f = 0.63$ and 1.44 are the tensile fracture strain of Domex Protect 500 and Wieldox 460 E steel, respectively.

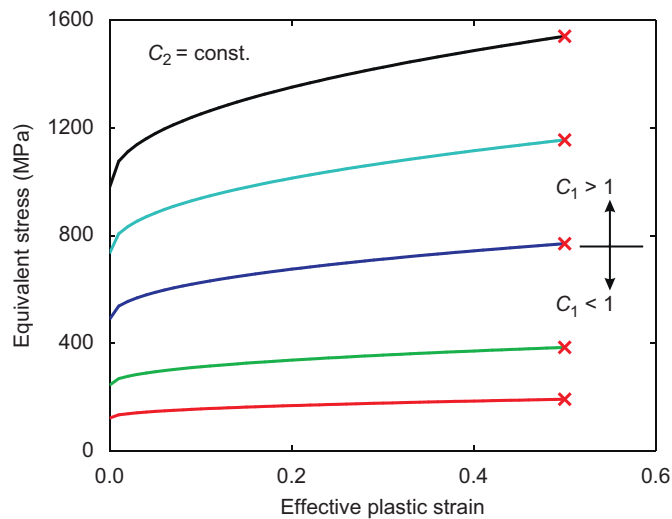


Fig. 4. Various stress–strain curves with the same fracture strain described by $\bar{\sigma} = C_1 f(\bar{\epsilon}_{pl})$.

3. Plasticity model

Consider the class of materials obeying the following hardening rule:

$$\bar{\sigma} = C_1 f(\bar{\epsilon}_{pl}) = C_1 [A + B \bar{\epsilon}_{pl}^n] \left[1 + C \ln \left(\frac{\dot{\bar{\epsilon}}_{pl}}{\dot{\bar{\epsilon}}_0} \right) \right] \left[1 - \left(\frac{T - T_0}{T_m - T_0} \right)^m \right], \quad (1)$$

where $\bar{\sigma}$ is the von Mises stress; $\bar{\epsilon}_{pl}$ is the effective plastic strain; A , B , n , C , and m are five material constants and need to be calibrated from tests; $\dot{\bar{\epsilon}}_{pl}$ and $\dot{\bar{\epsilon}}_0$ are the current and reference strain rate; T_m and T_0 are the melting and room temperature, respectively. The above equation describes the isotropic hardening, strain rate effects and

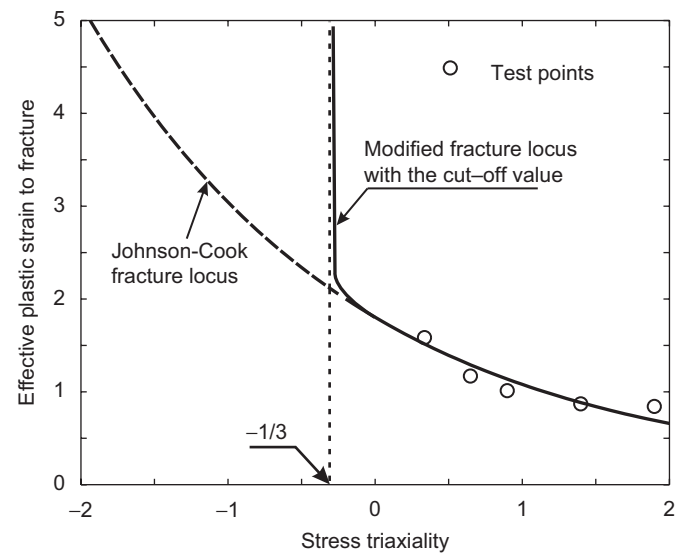


Fig. 5. Fracture loci for Wieldox 460 E steel, used in the present simulations.

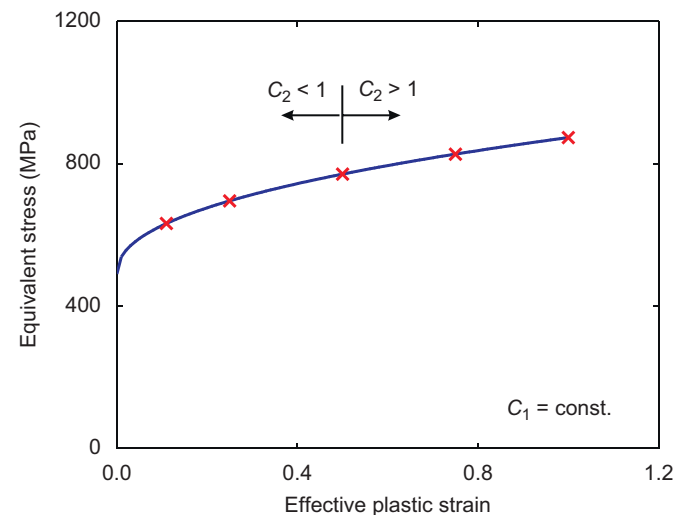


Fig. 6. The same stress–strain curves with various fracture strains.

temperature rise due to adiabatic heating [11]. The constant C_1 is introduced to differentiate materials within the entire class, $C_1 = 1$ being assigned to a reference material. Johnson and Cook [11] provided data for many materials.

For that reason, the simple separable hardening rule is often referred to as the Johnson–Cook plasticity model.

The reference material is Weldox 460 E steel. As a class of rolled steels manufactured by SSAB, Sweden, Weldox steel is of high strength and of outstanding ductility. To study the mechanical properties of Weldox 460 E steel, a series of static and dynamic tensile tests were conducted by Børvik et al. [12,13]. Table 1 gives the values of all of the material constants.

The plot of the quasi-static stress–strain curve of this material is shown in Fig. 3. Another commercial ultra high strength steel is Domex Protect 500, manufactured by the same company SSAB, Sweden. The quasi-static stress–strain curve of this material is also shown in Fig. 3. The extremely high strength of this material comes at the expense of a reduced ductility. The tensile fracture strain of Domex Protect 500 of $\bar{\epsilon}_f = 0.63$ is much smaller than that of Weldox 460 E steel of $\bar{\epsilon}_f = 1.44$. This property will be characterized in the next section. In general, one can introduce a class of hypothetical materials in which the hardening curve is of the same shape but different magnitudes, see Fig. 4.

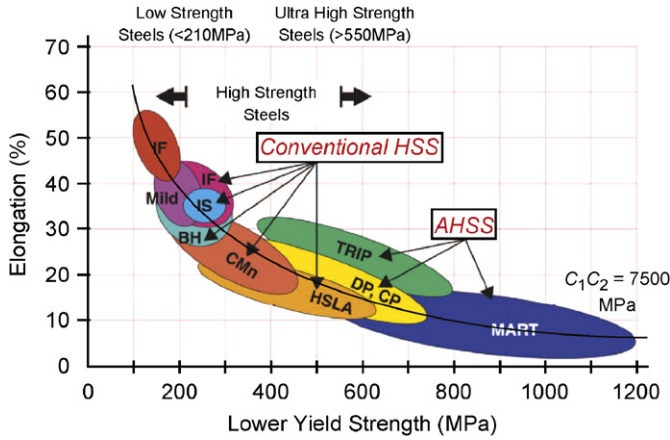


Fig. 7. Trade-off between strength and ductility.

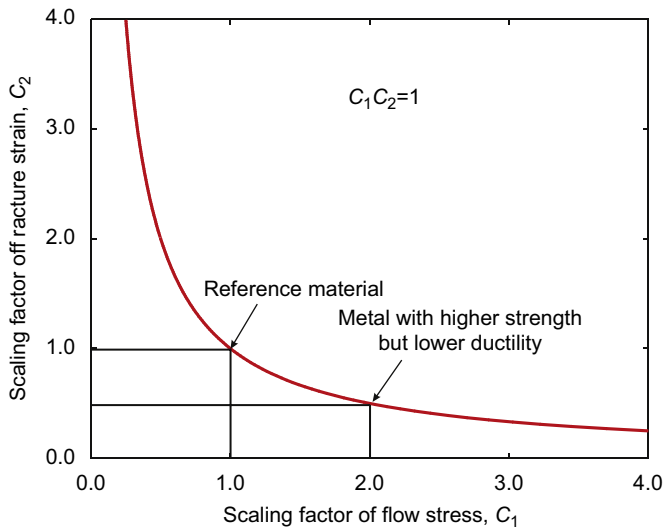


Fig. 8. A postulated relation between flow stresses and fracture strains.

4. Fracture model

The material failure will be formulated in terms of a macroscopic ductile fracture model recently proposed by Xue [14], Bao and Wierzbicki [15], Bai and Wierzbicki [16]. According to this model, the unknown equivalent strain to fracture at a material point is determined from the equation

$$D(\bar{\epsilon}_f) = 1, \tag{2}$$

where the damage indicator function $D(\bar{\epsilon}_f)$ is defined by

$$D(\bar{\epsilon}_f) = \int_0^{\bar{\epsilon}_f} \frac{d\bar{\epsilon}_{pl}}{\bar{\epsilon}_f^*(\xi, \eta)}. \tag{3}$$

In the above equation, the denominator $\bar{\epsilon}_f^*(\xi, \eta)$ is referred to as a 3-D fracture locus, calibrated from fracture tests under proportional loading. The arguments of the function $\bar{\epsilon}_f^*$ are the stress triaxiality η and the Lode angle parameter ξ ,

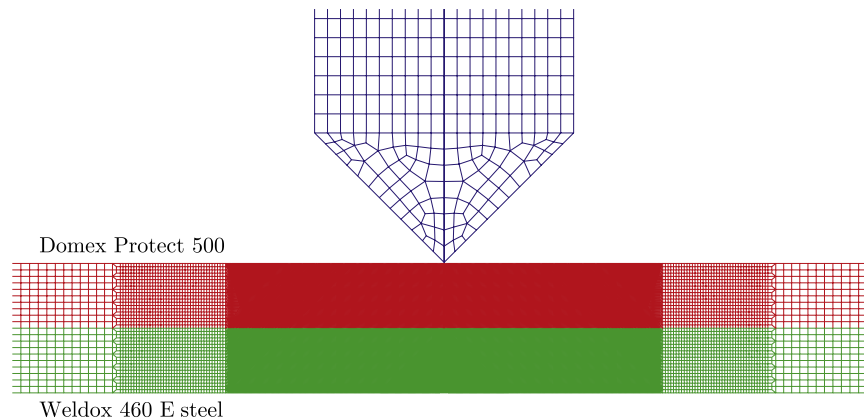


Fig. 9. The finite element model of a double-layered shield with different material combinations impacted by a conical-nose projectile. Hereinafter, Domex Protect 500 is described by red (dark) and Weldox 460 E steel is represented by green (shallow).

defined by

$$\eta = \frac{\sigma_m}{\bar{\sigma}}, \quad (4)$$

$$\xi = \frac{27 J_3}{2 \bar{\sigma}^{3/2}}. \quad (5)$$

A usual notation is used where σ_m is the mean stress and J_3 is the third invariant of the stress tensor. The correctness of the fracture criterion defined by Eqs. (2) and (3) was proved in laboratory tests, see Bai and Wierzbicki [16]. In numerical simulations of high velocity impact problems, a simplified fracture locus has been extensively used, e.g. Teng et al. [17] and Børvik et al. [9], by neglecting the dependence on the Lode angle parameter. For example, Børvik et al. [12,13] adopted the Johnson and Cook fracture model, in which the equivalent strain to fracture $\bar{\epsilon}_f$ depends only on the stress triaxiality:

$$\bar{\epsilon}_f = D_1 + D_2 \exp(D_3 \eta), \quad (6)$$

where D_1 , D_2 , and D_3 denote three material coefficients. Based on a series of tensile tests on round bars, Børvik et al. [12,13] obtained test data for Weldox 460 E steel: $D_1 = 0.0705$, $D_2 = 1.732$, and $D_3 = -0.54$. Actually, Johnson–Cook fracture loci calibrated from tensile tests are often extrapolated to the range of negative stress triaxialities in practical applications. Note that the ductility of materials under compression may then be underestimated due to the above extrapolation procedure. For the purpose of the present simulation, the Johnson–Cook fracture locus was modified by introducing a cut-off value for the negative stress triaxiality at $-\frac{1}{3}$, see Fig. 5. The concept of the cut-off value was first introduced by Bao and Wierzbicki [18] to describe the sharp increase of the ductility of materials under compression and takes indirectly into account the effect of the Lode angle parameter ξ . As demonstrated by Teng et al. [7,19], the cut-off value has a critical effect on the reconstruction of various fracture patterns in a number of high velocity impact problems. The ductility of

materials can be conveniently scaled by moving up and down the 2-D fracture locus, according to

$$\bar{\epsilon}_f = C_2 g\left(\frac{\sigma_m}{\bar{\sigma}}\right). \quad (7)$$

For a reference material (Weldox 460 E steel), the scaling parameter corresponding to a uniaxial tensile fracture is taken to be $C_2 = 1$. A hypothetical class of materials with the same magnitude and shape of the stress–strain curve but various fracture strains are shown in Fig. 6.

In reality there is a trade-off between the strength and ductility. This is illustrated in Fig. 7 showing the range of the engineering fracture strain and the yield stress for several commonly encountered steels. The above “banana” type of trend can be well described by a hyperbolic function: $C_1 C_2 = \text{const}$, which is plotted in Fig. 8. If the

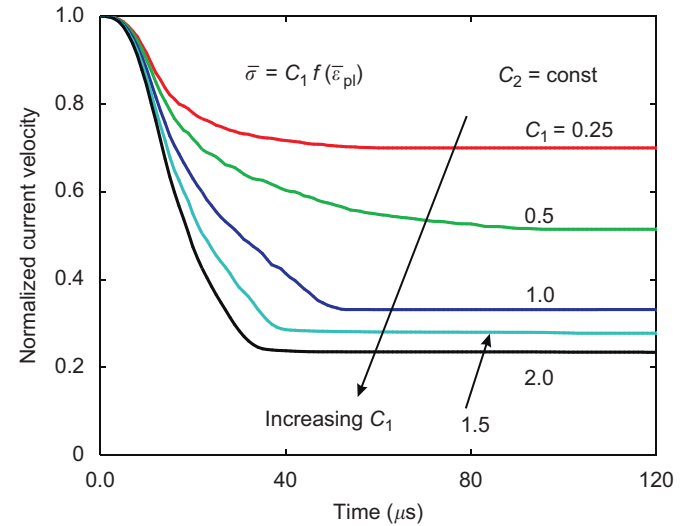


Fig. 11. Time history of the normalized transient velocity of the projectile for the case with the different stress–strain curves and the same fracture strain.

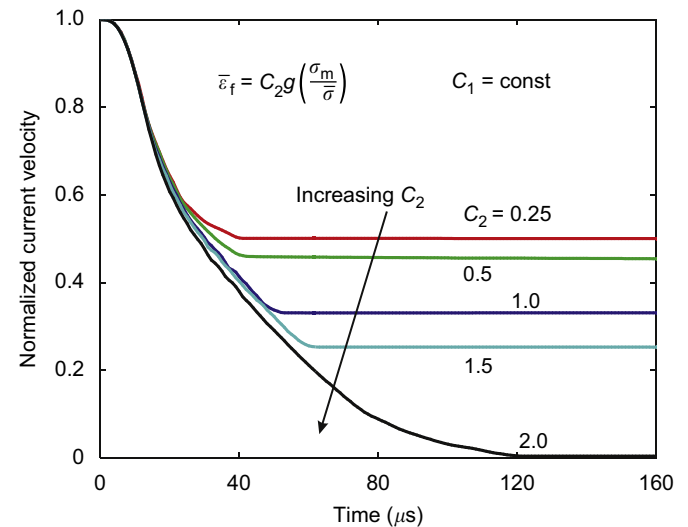


Fig. 12. Time history of the transient velocity of the projectile for the case with different ductility and the same stress–strain curve.

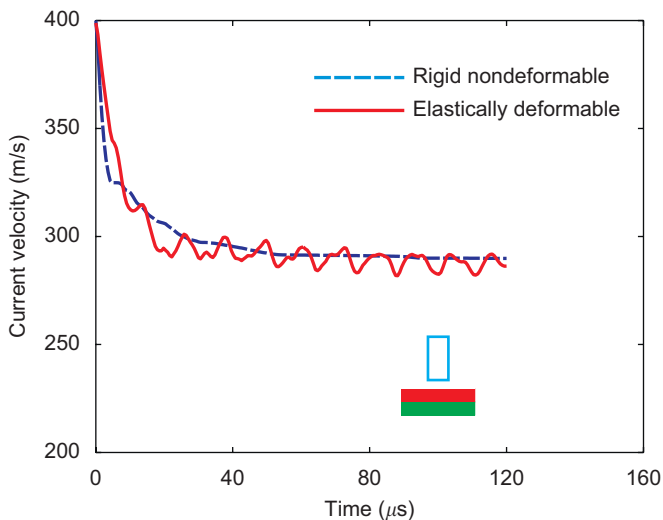


Fig. 10. Comparison of the time history of the transient velocity of the heavy flat-nose projectile impacted against the double-layered shield at $V_0 = 400$ m/s.

Weldox 460 E is taken as a reference material, then the ductility scaling parameter for the Domex with $C_1 = 2.5$ should be $C_2 = 1/2.5 = 0.4$. From Fig. 3, the ratio of ductility of Weldox to Domex is $(C_2)_{exp} = 0.43$, which is very close to the theoretically calculated value based on the empirical equation: $C_1 C_2 = const$. It can be concluded that the above two types of armor steels follow the simple scaling trade-off between strength and ductility.

5. Computational model

The case with the monolithic plate will be considered as a reference. Two materials of different ductility and strength

are designed for the two layers of the double-layered shields. In our simulations, the radius of the circular plate is 250 mm and the equivalent total thickness is 12 mm. Clamped boundary condition are assumed at the periphery of the plate. However, for the assumed dimensions of the plate, the local perforation process will not be affected by the far field boundary conditions. The interface between two layers is represented by node continuity. In other words, the two materials are considered as welded together, thus transmitting shear and tensile stresses in addition to compression.

A 2-D finite element model was generated for each projectile–target shield system. For the case with the monolithic and the double-layered shields, the circular plates were modeled using four-node, axisymmetric elements with reduced integration (CAX4R). Fig. 9 shows a finite element model for the double-layered shield with two different materials, in which Domex Protect 500 and Weldox 460 E steel are represented, respectively, by red and green. This notation will be used hereinafter. The element size is 0.2×0.2 mm in the impacted zone right below the projectile, see Fig. 9. An early study indicates that numerical simulations based on such an element size agree well with experimental results [20]. The errors between numerically predicted ballistic limits and those obtained from tests were always less than 10% [20].

The projectiles were considered to be elastically deformable in our simulations. In reality, a projectile would absorb some kinetic energy in the form of plastic deformation and may break into pieces under shock wave loading, e.g. see Børvik et al. [21]. For simplicity, the projectile can even be represented by a rigid body. Although with this assumption stress wave propagation

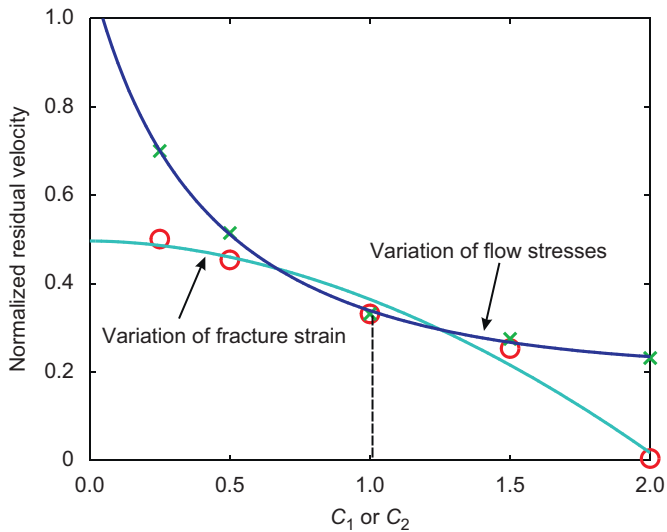


Fig. 13. Normalized residual velocities vs. scaling parameters of yield strength and fracture strain.

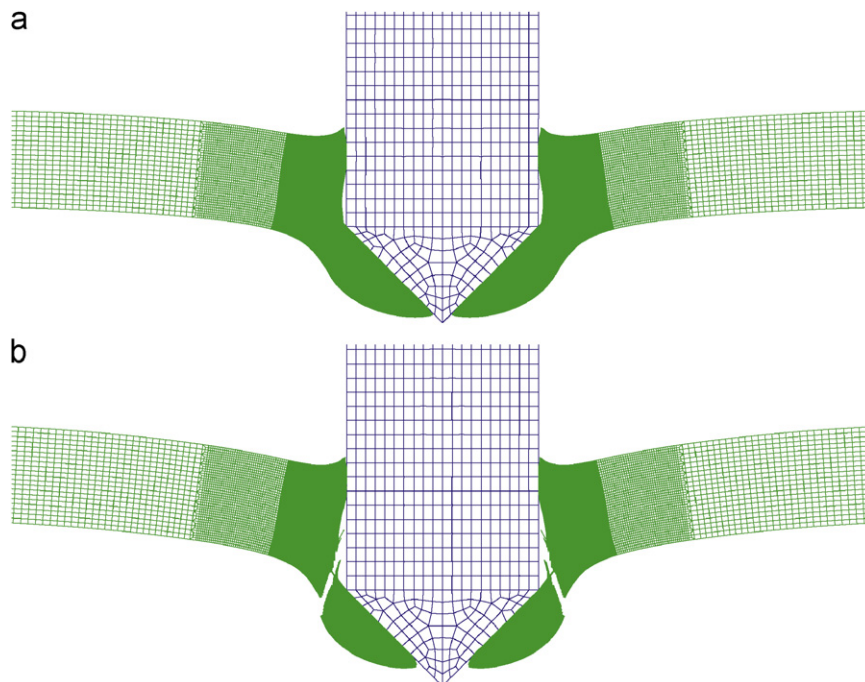


Fig. 14. Perforation process of the monolithic plate of high ductility material impacted by the heavy conical-nose projectile at $V_0 = 400$ m/s.

cannot be correctly modeled, the calculated residual velocity is close to the one with the elastic projectile, see Fig. 10 for one example.

Also, we have to correctly define the contact conditions between any two bodies because they may interact with each other. For the monolithic plates, the kinematic contact constraint was defined between the projectile and the impacted zone of the target shields. The problem becomes much more complex for the case with the double-layered shields. Obviously, the projectiles may sequentially get into contact with each layer and meanwhile the layers may interact with each other. The kinematic contact

constraints were defined between the projectile and each layer. For all of the possible contact interfaces, a constant frictional coefficient 0.1 was defined.

6. Simulation with varying either strength or ductility

The perforation resistance of the monolithic plate varies with strength and ductility of the material. At first, the fracture strain is maintained to be the same, while the stress–strain curve is scaled with the baseline stress–strain curve. Another limiting case is scaling the fracture strain and maintaining the stress–strain curve the same. Figs. 11

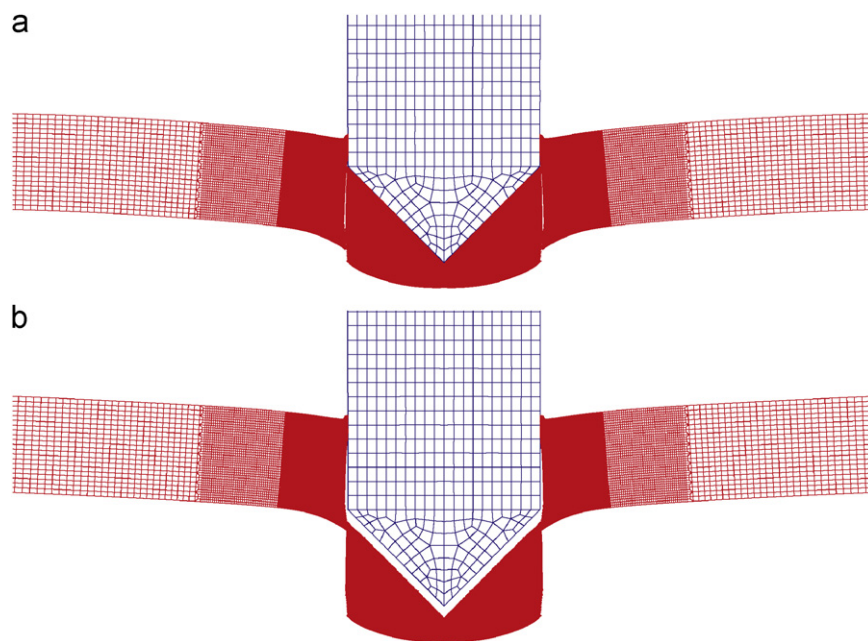


Fig. 15. Perforation process of the monolithic plate of low ductility material impacted by the heavy conical-nose projectile at $V_0 = 400$ m/s.

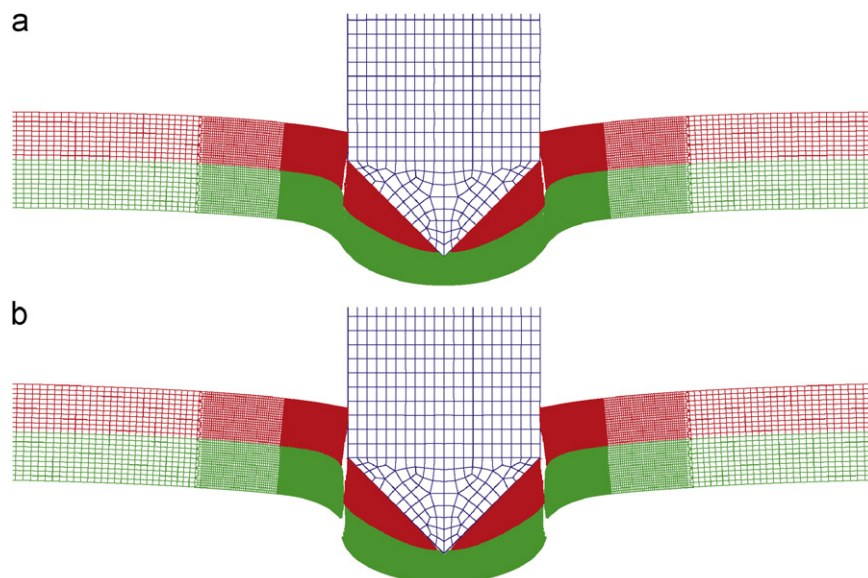


Fig. 16. Perforation process of the double-layered shield with the upper layer of low ductility material and the lower layer of high ductility material impacted by the heavy conical-nose projectile at $V_0 = 400$ m/s.

and 12 show, respectively, the time history of the velocity of the projectile for the two cases. A plot of the normalized residual velocities of the projectile vs. the scaling parameters C_1/C_2 is shown in Fig. 13. It is understood that varying one parameter (C_1 or C_2) at a time may be unrealistic, because as shown in Fig. 7, strength and ductility are related. However, such an analysis clearly shows and quantifies the trends.

7. Ballistic resistance of double-layered shields with two different materials

7.1. Heavy conical-nose projectile

In this section, a conical-nose projectile of the mass $M_0 = 200$ g and the diameter $d = 24$ mm is considered as the striker. At first, the monolithic plate of the same material, Weldox 460 E steel or Domex Protect 500 steel, is studied. Figs. 14 and 15 show the final stage of the perforation processes of the monolithic plates of high ductility and low ductility materials, respectively, impacted by the heavy conical-nose projectile at $V_0 = 400$ m/s.

As shown in Fig. 15, shear plugging is the predominant failure mode for the monolithic plate of low ductility material. Since the monolithic plate of high ductility material undergoes deep necking before failure, its dominant failure mode is plastic indentation followed by tensile tearing, see Fig. 14. Compared with high ductility material Weldox 460 E steel, the low fracture locus of Domex Protect 500 steel leads to early fracture and insignificant global deformation. It can be concluded that high ductility material has advantage over low ductility

material in terms of energy dissipation. Actually, the contribution of low ductility material to plastic energy dissipation is weakened by its early fracture.

Now, the following question arises: How to maximize the energy dissipation potential of low ductility material. It is suggested that a double-layered shield with the upper and lower layer of different materials be considered as a possible optimum configuration of the shield for ballistic resistance.

Fig. 16 shows the perforation processes of the double-layered shield with the upper layer of low ductility material and the lower layer of high ductility material impacted by

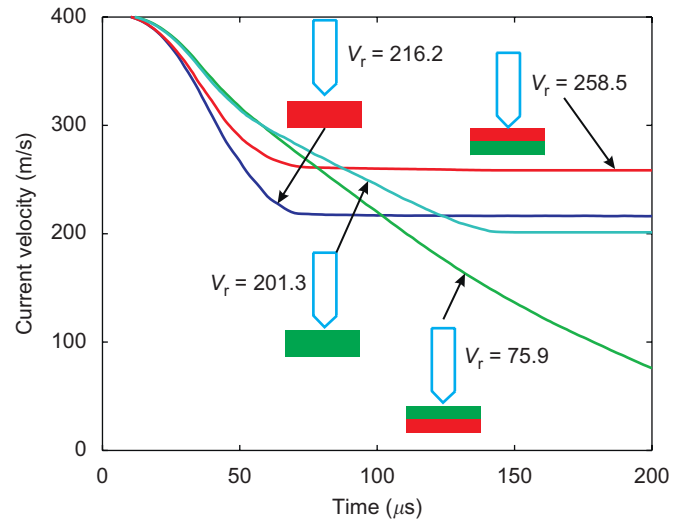


Fig. 18. Time history of the transient velocity of the heavy conical-nose projectile at $V_0 = 400$ m/s. Here V_r is the residual velocity with unit m/s.

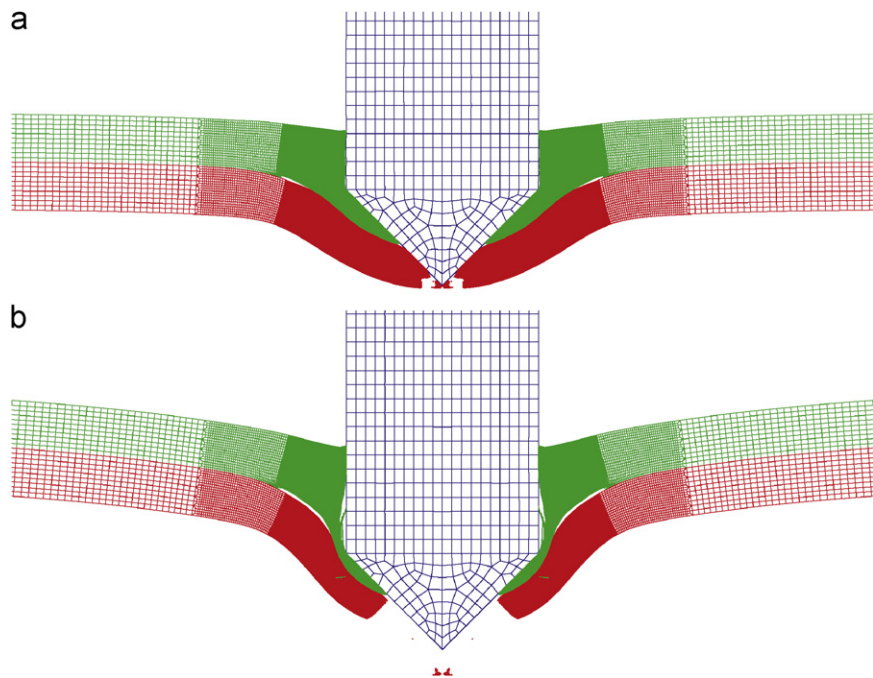


Fig. 17. Perforation process of the double-layered shield with the upper layer of high ductility material and the lower layer of low ductility material impacted by the heavy conical-nose projectile at $V_0 = 400$ m/s.

the heavy conical-nose projectile at $V_0 = 400$ m/s. It can be observed that the upper layer tends to fail by shear plugging with insignificant global bending and plastic deformation. This is similar to the preceding case with the monolithic plate of the low ductility material. This configuration is not able to improve the perforation resistance.

Now, by exchanging the position of two materials, another modified configuration is obtained. Fig. 17 shows the perforation process of the double-layered shield with the upper layer of high ductility material and the lower

layer of low ductility material impacted by the heavy conical-nose projectile at $V_0 = 400$ m/s. Note that the respective strengths of the materials are inversely proportional to the ductility.

It can be observed from Fig. 17 that the upper layer undergoes deep indentation followed by necking before failure. Therefore, the predominant failure mode for the upper layer is tensile tearing, while the lower layer mainly fails by shear plugging. Since the deformation region is extended well beyond the impacted zone, the global bending in this configuration is found to be larger than

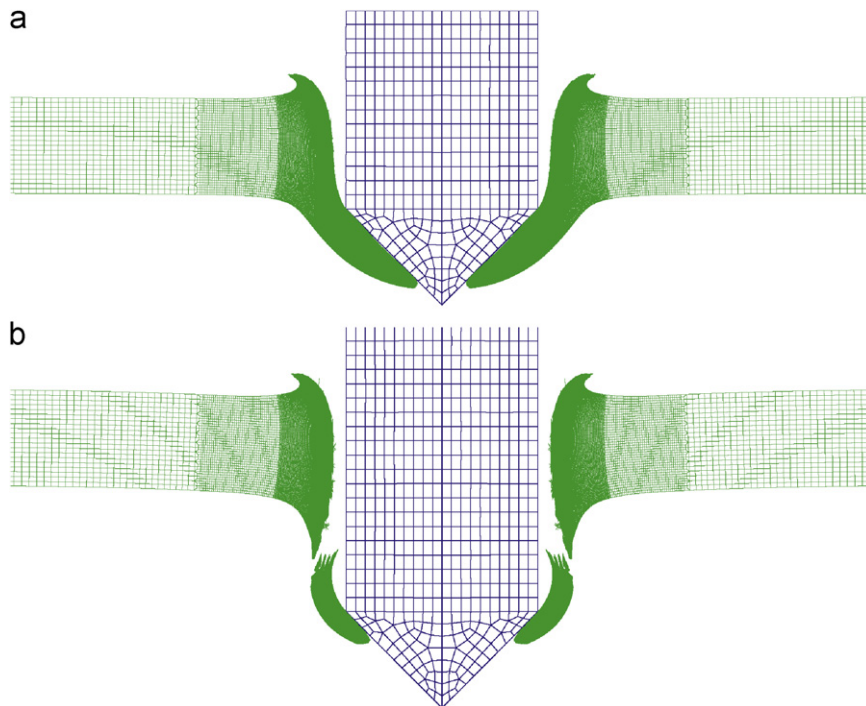


Fig. 19. Perforation process of the monolithic plate of high ductility material impacted by the heavy conical-nose projectile at $V_0 = 800$ m/s.

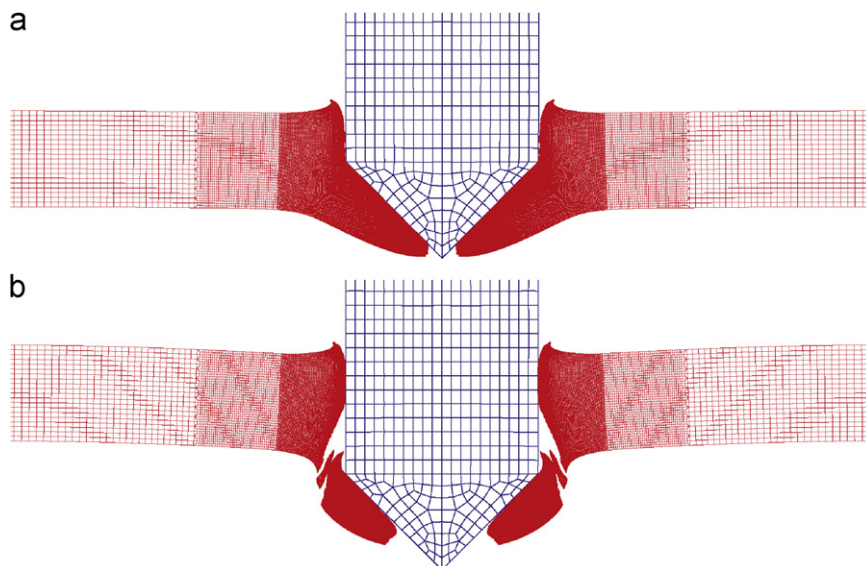


Fig. 20. Perforation process of the monolithic plate of low ductility material impacted by the heavy conical-nose projectile at $V_0 = 800$ m/s.

that in any other configurations. The transition of the failure mode from shear plugging to tensile tearing is accompanied by a considerable increase in plastic energy dissipation. It can be concluded that the best configuration for the perforation resistance against the heavy conical-nose projectile at $V_0 = 400$ m/s is the double-layered shield with the upper layer of high ductility and lower strength material and the lower layer of low ductility and high strength material. Fig. 18 shows the time history of the transient velocity for these four cases. The simulation

results are in general in accordance with our qualitative analysis.

How will the above picture change with a higher impact velocity, e.g. $V_0 = 800$ m/s? Figs. 19–22 show the perforation processes of the four shields impacted by the heavy conical-nose projectile at $V_0 = 800$ m/s.

It can be observed that, a high velocity increases the local plastic deformation in the impacted zone in all configurations. The failure mode is tensile tearing for the monolithic plate and the double-layered shield with

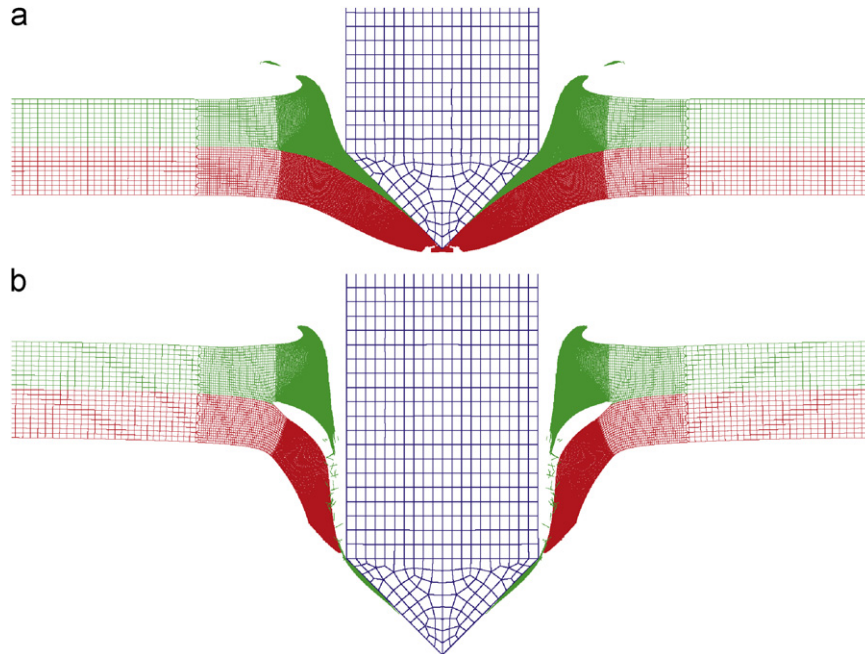


Fig. 21. Perforation process of the double-layered shield with the upper layer of high ductility material and the lower layer of low ductility material impacted by the heavy conical-nose projectile at $V_0 = 800$ m/s.

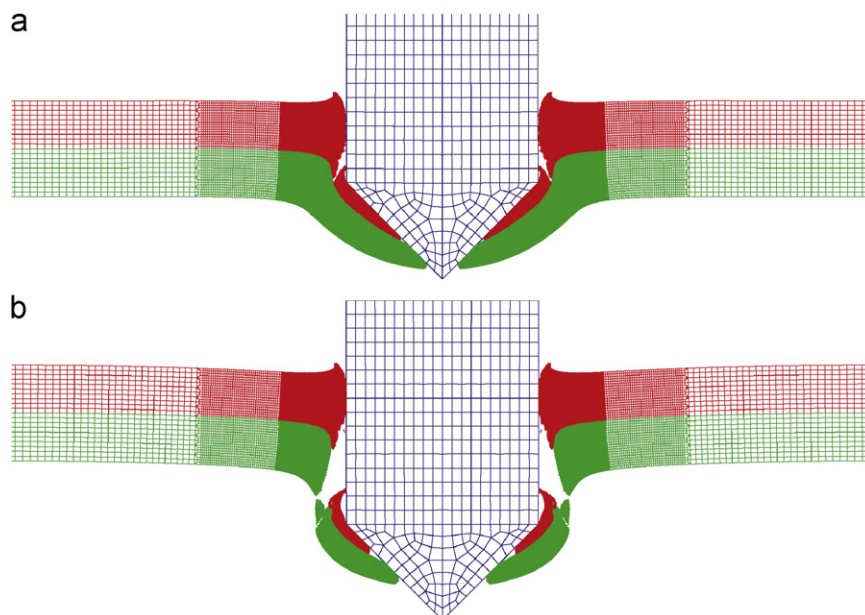


Fig. 22. Perforation process of the double-layered shield with the upper layer of low ductility material and the lower layer of high ductility material impacted by the heavy conical-nose projectile at $V_0 = 800$ m/s.

the upper layer of high ductility material and the lower layer of low ductility material, while the double-layered shield with the upper layer of low ductility material and the lower layer of high ductility material mainly fails by shear plugging. At $V_0 = 800$ m/s, the perforation resistance depends strongly on the strength of the materials, see Fig. 23.

7.2. Heavy flat-nose projectile

The projectile considered in this section is of a flat-nose and of the same mass $M_0 = 200$ g and the diameter $d = 24$ mm. Impacted by the heavy flat-nose projectile, the failure mode of the four shields are nearly the same, that is, shear plugging. As an example, Fig. 24 shows the perforation processes of the double-layered shield with the upper layer of high ductility material and the lower layer of low ductility material impacted by the heavy flat-nose projectile at $V_0 = 400$ m/s.

It can be observed that shear plugging is the predominant failure mode for all the four configurations. Crack formation and propagation is often induced by the sharp corner of the flat-nose projectile. Also, the shields undergo insignificant global deformation and the plastic deformation is localized in the impacted zone. Yet, the double-layered shield with the upper layer of high ductility material and the lower layer of low ductility material is again the best in perforation resistance among all the configurations. This can be seen from the time history of the transient velocity of the heavy flat-nose projectile, see Fig. 25. Physically, the gain in the perforation resistance is caused in this case by the round-off edges of the upper layer plug.

At the impact velocity of 800 m/s, the phenomenon becomes more interesting. As shown in Figs. 26–29, the materials in the impacted zone are push aside and a cavity, whose diameter is larger than that of the projectile, is generated. As a projectile approaches the rear surface of

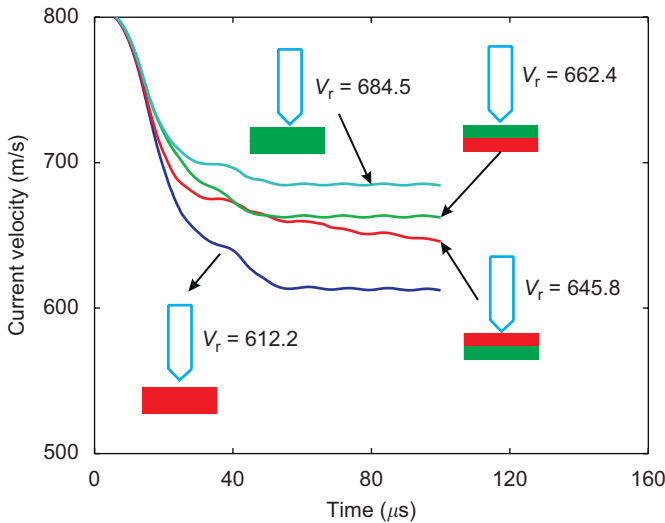


Fig. 23. Time history of the transient velocity of the heavy conical-nose projectile at $V_0 = 800$ m/s.

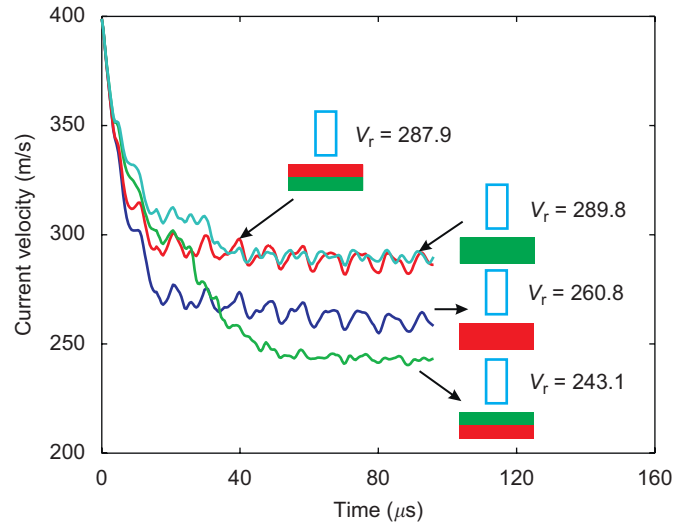


Fig. 25. Time history of the transient velocity of the heavy flat-nose projectile at $V_0 = 400$ m/s.

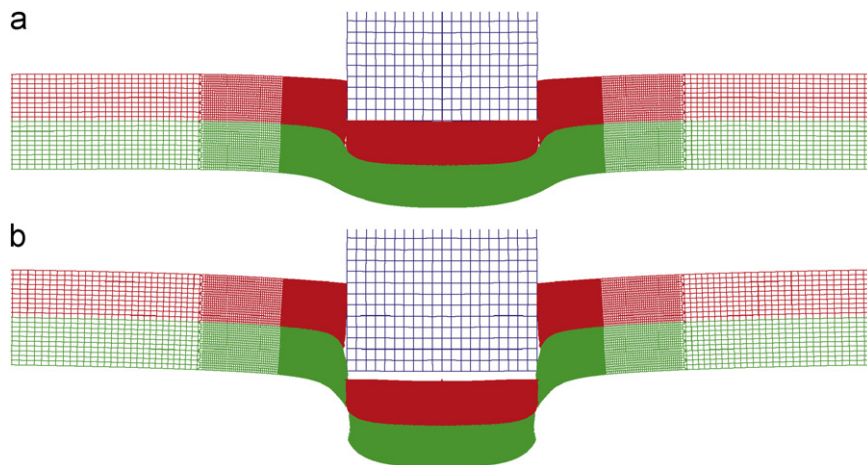


Fig. 24. Perforation process of the double-layered shield with the upper layer of low ductility material and the lower layer of high ductility material impacted by the heavy flat-nose projectile at $V_0 = 400$ m/s.

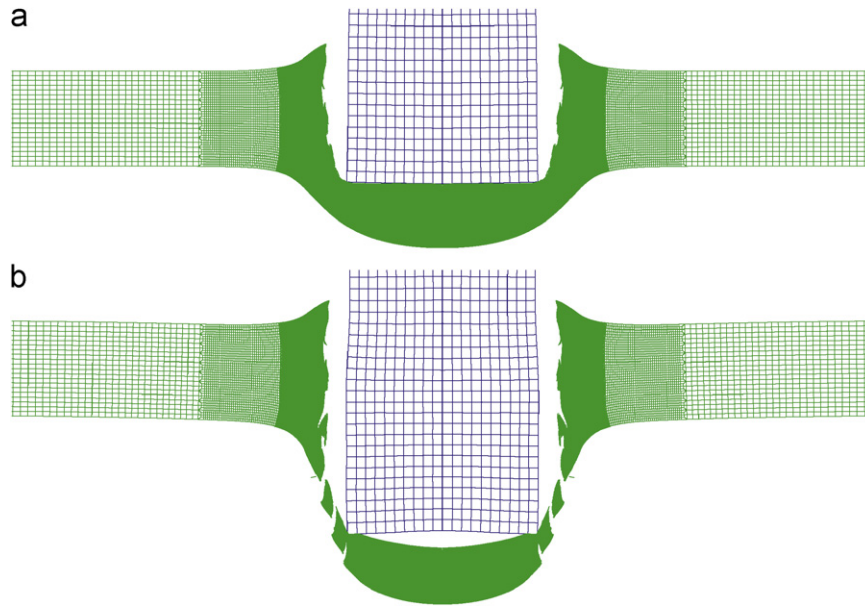


Fig. 26. Perforation process of the monolithic plate of high ductility material impacted by the heavy flat-nose projectile at $V_0 = 800$ m/s.

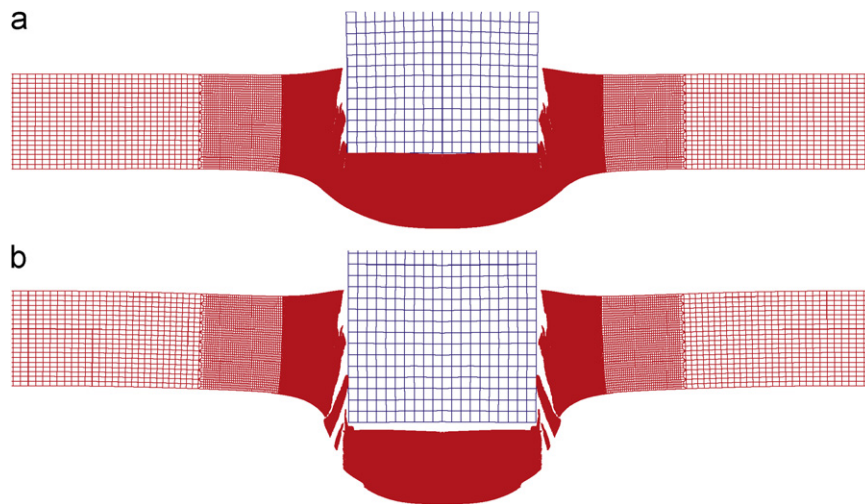


Fig. 27. Perforation process of the monolithic plate of low ductility material impacted by the heavy flat-nose projectile at $V_0 = 800$ m/s.

the shields, the failure mode changes to tensile tearing. Fig. 30 shows the time history of the transient velocity of the heavy flat-nose projectile. It is found that, the perforation resistance of the shields are almost the same at $V_0 = 800$ m/s.

7.3. Light conical-nose projectile

In this section, a conical-nose projectile of the mass $M_0 = 30$ g and the diameter $d = 12$ mm is considered as the striker. Since the light projectile will be stopped by all type of shields at the impact velocity of 400 m/s, a high impact velocity, e.g. $V_0 = 800$ m/s, is required to differentiate the perforation resistance of the four types of shields. The perforation processes of the shields impacted by the light conical-nose projectile are similar to that for the heavy

conical-nose projectile at $V_0 = 800$ m/s. Fig. 31 shows the time history of the transient velocity of the light conical-nose projectile impacted at the four types of the shields at $V_0 = 800$ m/s.

7.4. Light flat-nose projectile

In this section, a flat-nose projectile of the mass $M_0 = 30$ g and the diameter $d = 12$ mm is considered. At $V_0 = 400$ and 800 m/s, the perforation processes of the shields impacted by the flat-nose projectile are similar to that impacted by the heavy flat-nose projectile.

The time histories of the transient velocity of the light flat-nose projectile impacted at the four types of shields at $V_0 = 400$ and 800 m/s are summarized in Figs. 32 and 33. According to our simulation results, the double-layered

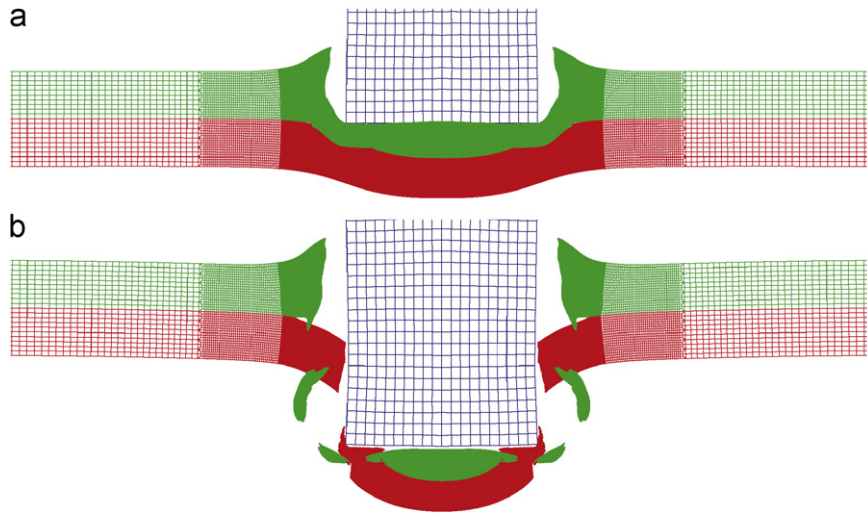


Fig. 28. Perforation process of the double-layered shield with the upper layer of high ductility material and the lower layer of low ductility material impacted by the heavy flat-nose projectile at $V_0 = 800$ m/s.

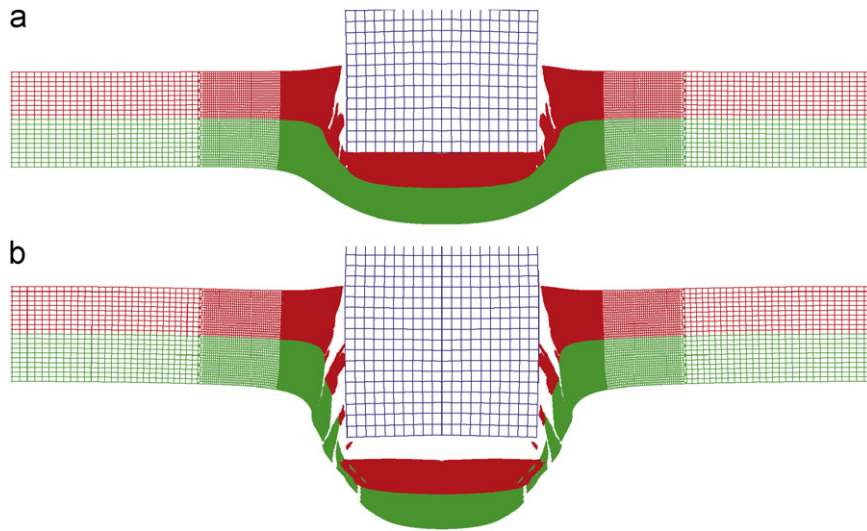


Fig. 29. Perforation process of the double-layered shield with the upper layer of low ductility material and the lower layer of high ductility material impacted by the heavy flat-nose projectile at $V_0 = 800$ m/s.

shield with the upper layer of high ductility material and the lower layer of low ductility material is the best configuration in perforation resistance among all types of shields at $V_0 = 400$ m/s. At $V_0 = 800$ m/s, the double-layered shield with the upper layer of high ductility material and the lower layer of low ductility material is as effective as the monolithic plate made of high strength material.

8. Two layers with gap

In the present study, the two layers made of the two different metals are assumed to be perfectly bonded. The displacement field across the interface is continuous and all the stress components can be transferred between the two layers. Recent investigations by Teng et al. [17] and Dey

et al. [5] reveal that the perforation resistance of a target can be improved by about 7–25% by simply laminating the two layers without any adhesion. The two layers were made of the same metal and there was no interaction between the layers in terms of tension and shear. The results lead to an interesting question: Can the ballistic limits of a target be further improved by combining the two independent concepts of two separated layers made of two different grade metals? A pilot study was conducted by performing additional numerical simulation at $V_0 = 400$ m/s for the heavy projectile and at $V_0 = 800$ m/s for the light projectile. The calculation results are summarized in Table 2. It can be seen that the residual velocities in the cases with the separated layers are always lower than, or close to, those in the corresponding cases with the perfectly bonded plates. It indicates that the combined use of the

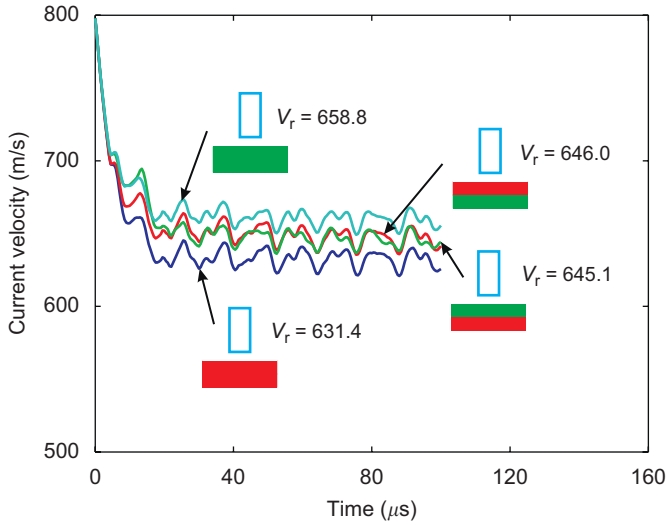


Fig. 30. Time history of the transient velocity of the heavy flat-nose projectile at $V_0 = 800$ m/s.

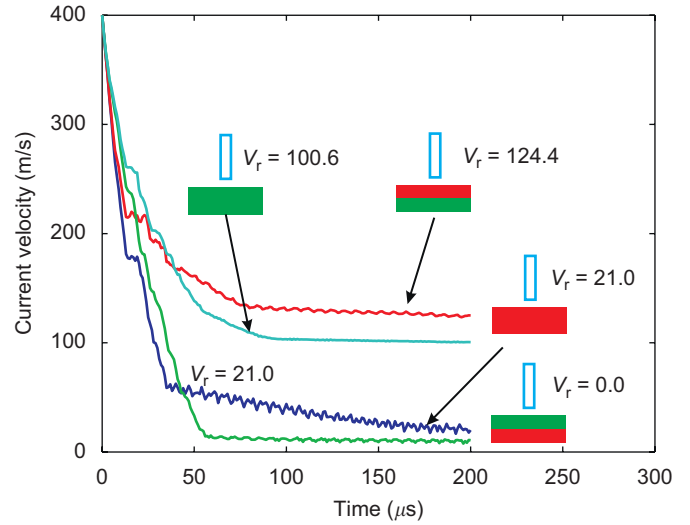


Fig. 32. Time history of the transient velocity of the light flat-nose projectile at $V_0 = 400$ m/s.

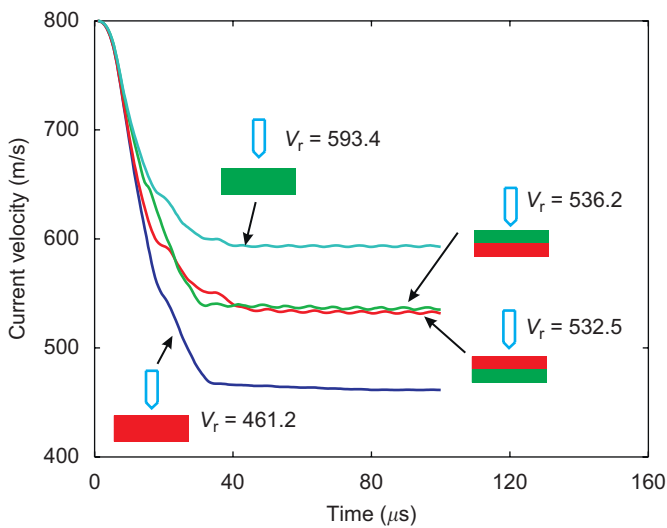


Fig. 31. Time history of the transient velocity of the light conical-nose projectile at $V_0 = 800$ m/s.

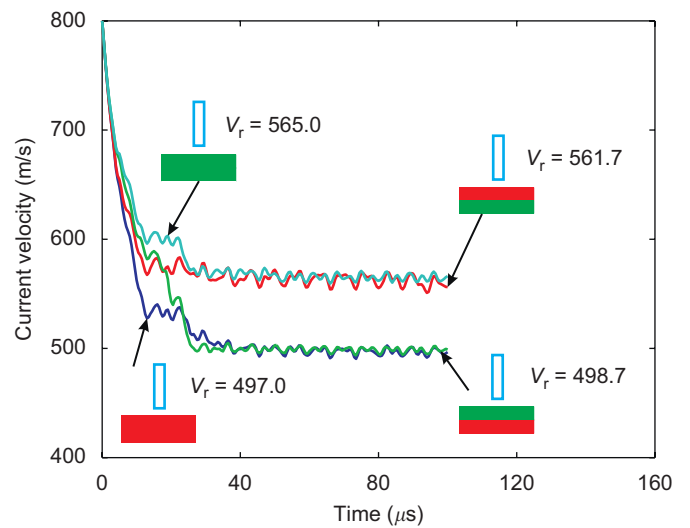


Fig. 33. Time history of the transient velocity of the light flat-nose projectile at $V_0 = 800$ m/s.

separation and different metals is promising. A systematic study covering a wide range of initial impact velocities and different types of projectile noses is underway, which will give us more confidence of the optimization of the armor plate.

9. Conclusions and discussions

At low impact velocities, the double-layered shield with the upper layer of high ductility metal and the lower layer of low ductility and high strength metal is always the best configuration for the perforation resistance among the four configurations, while the double-layered shield with the upper layer of low ductility material and the lower layer of high ductility material is the worst one.

Under high velocity impact by the heavy flat-nose projectile, which is the most detrimental projectile, the four configurations are nearly the same in the perforation resistance. Under high velocity impact by the heavy conical-nose projectile and the light flat-nose projectile, which are the medium detrimental projectiles, the perforation resistance mainly depends on the ductility, while the effect of the configuration is small. Under high velocity impact by the light conical-nose projectile, which is the least detrimental projectile, the double-layered shield with the upper layer of high ductility material and the lower layer of low ductility material is superior to the other three configurations in the perforation resistance.

The kinetic energy of the projectile is dissipated in four types of forms: plastic indentation in the impacted zone

Table 2
Comparison of residual velocities between the bonded and the separated cases

Shields	Heavy conical-nose		Heavy flat-nose		Light conical-nose		Light flat-nose	
	Bonded	Separated	Bonded	Separated	Bonded	Separated	Bonded	Separated
	216.2	9.2	260.8	233.8	461.2	468.9	497.0	497.7
	258.5	234.4	287.9	289.0	532.5	539.9	561.7	555.7
	75.9	11.7	243.1	222.3	536.2	520.3	498.7	497.0
	201.3	192.4	289.8	280.7	593.4	584.4	565.0	567.2

right below the projectile, necking deformation and tensile tearing, through-thickness shear plugging, and global bending deformation. The ratios among them change with the mass and shape of the projectile and the configuration of the target. This leads to different effectiveness of the double-layered shield in the perforation resistance for various projectiles.

It can be concluded that, an armor plate made of two different metallic materials is an interesting alternative to the concept of a ceramic armor backed by a metal plate. Note that in the present study the erosion and fracture of the projectiles have not been taken into account. The conclusion should be applied to thin or intermediately thick armor shields under sub-ordnance velocity impact, in which a projectile is relatively strong and is able to keep intact. Under ordnance velocity impact, ceramic-faced armor shields may be more effective in the perforation resistance by eroding a projectile than the present configuration.

References

- [1] Marom I, Bodner SR. Projectile perforation of multilayered beams. *Int J Mech Sci* 1979;21(8):489–504.
- [2] Corran RSJ, Shadbolt PJ, Ruiz C. Impact loading of plates—an experimental investigation. *Int J Impact Eng* 1983;1(1):3–22.
- [3] Radin J, Goldsmith W. Normal projectile penetration and perforation of layered targets. *Int J Impact Eng* 1988;7(2):229–59.
- [4] Almohandes AA, Abdel-Kader MS, Eleiche AM. Experimental investigation of the ballistic resistance of steel-fiberglass reinforced polyester laminated plates. *Compos Part B: Eng* 1996;27(5):447–58.
- [5] Dey S, Børvik T, Teng X, Wierzbicki T, Hopperstad OS. On the ballistic resistance of double-layered steel plates: an experimental and numerical investigation. *Int J Solids Struct* 2007;44:6701–23.
- [6] Børvik T, Dey S, Clausen AH. A preliminary study on the perforation resistance of high-strength steel plates. *J Phys IV* 2006;134:1053–9.
- [7] Teng X, Wierzbicki T. Failure mode transition in round-nosed mass-to-beam impact. *Eur J Mech—A Solids* 2005;24(5):857–76.
- [8] Børvik T, Langseth M, Hopperstad OS, Malo KA. Perforation of 12 mm thick steel plates by 20 mm diameter projectiles with flat, hemispherical and conical noses. Part I: experimental study. *Int J Impact Eng* 2002;27(1):19–35.
- [9] Børvik T, Hopperstad OS, Berstad T, Langseth M. Perforation of 12 mm thick steel plates by 20 mm diameter projectiles with flat, hemispherical and conical noses. Part II: numerical simulations. *Int J Impact Eng* 2002;27(1):37–64.
- [10] Military Specification MIL-P-46593A (ORD). Projectile, calibers 0.22, 0.30, 0.50, and 20-mm fragment simulating, 1962.
- [11] Johnson GR, Cook WH. A constitutive model and data for metals subjected to large strains, high strain rates and high temperatures. In: *Proceedings of the seventh international symposium on ballistics*, Hague, Netherlands, 1983. p. 541–7.
- [12] Børvik T, Hopperstad OS, Berstad T, Langseth ML. A computational model of viscoplasticity and ductile damage for impact and penetration. *Eur J Mech: A/Solids* 2001;20:685–712.
- [13] Børvik T, Hopperstad OS, Dey S, Pizzinato EV, Langseth M, Albertini C. Strength and ductility of Weldox 460 E steel at high strain rates, elevated temperatures and various stress triaxialities. *Eng Fract Mech* 2005;72:1071–87.
- [14] Xue L. Damage and fracture initiation of uncracked ductile solids under triaxial loading. *Int J Solids Struct* 2007;44:5163–88.
- [15] Bao Y, Wierzbicki T. On fracture locus in the equivalent strain and stress triaxiality space. *Int J Mech Sci* 2004;46(1):81–98.
- [16] Bai Y, Wierzbicki T. A new model of metal plasticity and fracture with pressure and Lode dependence. *Int J Plasticity*, 2007, accepted for publication.
- [17] Teng X, Dey S, Børvik T, Wierzbicki T. Protection performance of double-layered metal shields against projectile impact. *J Mech Mater Solids* 2007;2:1307–28.
- [18] Bao Y, Wierzbicki T. On the cut-off value of negative triaxiality for fracture. *Eng Fract Mech* 2005;72(7):1049–69.
- [19] Teng X, Wierzbicki T, Hiermaier S, Rohr I. Numerical prediction of the Taylor test with fracture. *Int J Solids Struct* 2005;42(9/10):2929–48.
- [20] Teng X, Wierzbicki T. Numerical study on crack propagation in high velocity perforation. *Comput Struct* 2005;83:989–1004.
- [21] Børvik T, Hopperstad OS, Langseth M, Malo KA. Effects of target thickness in blunt projectile penetration of Weldox 460 E steel plates. *Int J Impact Eng* 2003;28(4):413–64.